Identification of large coherent structures in supersonic axisymmetric wakes

D.A. von Terzi[a,†], R.D. Sandberg[b], H.F. Fasel[c]

[a] *Institut für Thermische Strömungsmaschinen, Universität Karlsruhe, D-76128 Karlsruhe, Germany*
[b] *School of Engineering Sciences, University of Southampton, Southampton SO17 1BJ, U.K.*
[c] *Department of Aerospace and Mechanical Engineering, The University of Arizona, Tucson AZ 85721, USA*

[†]Corresponding author. Tel.: +49-721-608-6829; fax: +49-721-608-2767.
E-mail address: dominic.vonterzi@its.uni-karlsruhe.de (D.A. von Terzi)

Abstract

Direct numerical simulation data of supersonic axisymmetric wakes are analysed for the existence of large coherent structures. Wakes for a range of Reynolds numbers at $Ma = 2.46$ are considered with results being presented for cases at $Re_D = 30,000$ and 100,000. Criteria for identification of coherent structures in free-shear flows found in the literature are compiled and discussed, and the role of compressibility is addressed. In particular, the ability and reliability of visualisation techniques intended for incompressible shear-flows to educe meaningful structures in supersonic wakes is scrutinised. It is shown that some of these methods retain their usefulness for identification of vortical structures whose swirling rate is larger than the local compression and expansion rates in the flow field. Best 'visibility' of coherent structures is achieved by employing visualisation techniques and proper orthogonal decomposition in combination with the introduction of artificial perturbations (forcing of the wake). The existence of both helical and longitudinal structures in the shear layer and of hairpin-like structures in the developing wake is demonstrated. In addition, elongated tubes of streamwise vorticity are observed to emanate from the region of recirculating flow.

Keywords: supersonic axisymmetric wakes; compressible vortex identification; coherent structures; flow visualisation; direct numerical simulation

1 Introduction

The existence of large-scale orderly structures in turbulent free-shear flows, commonly called large coherent structures, has long been established in the literature, e.g. for jets by Crow & Champagne [1], for mixing-layers by Brown & Roshko [2], for plane wakes by Wygnanski *et al.* [3] and for axisymmetric wakes by Cannon *et al.* [4] to name only a few. These structures are assumed to dominate the momentum transfer between different flow regions and to have a significant impact on noise generation, drag, heat transfer, and mixing. For this reason, predicting and possibly controlling the behaviour of large coherent structures in free-shear flows is of great interest. A prerequisite for accurate predictions is an unambiguous identification of these structures. Identified structures may then be tracked and their evolution studied. Furthermore, knowledge about the physical mechanism which governs the generation of a specific structure might be gained once the origin of the structure is localised. Clearly, understanding the physical processes of coherent structure generation will benefit the development of

flow control methods.

A prototypical configuration for which many flow control techniques are tested is the supersonic axisymmetric wake. Methods employed include boat-tailing [5, 6, 7, 8], base-bleeding [9, 10, 11], or active flow control [12]. Unfortunately, a reliable identification of the inherently three-dimensional coherent structures in this flow is difficult. Experiments are currently restricted to planar visualisations and statistical correlations whereas numerical simulations have so far been dependent on turbulence modelling approaches. For such simulations at best only the largest structures can be computed while there is no guarantee that all relevant structures are resolved and that those captured are computed in sufficient accuracy. For the turbulent supersonic axisymmetric wake, turbulence modelling deficiencies and lack of resolution are commonly deemed responsible for the observed discrepancies of simulations compared to experiments in predicting global mean flow quantities like the base pressure and/or the length of the recirculation zone [13]. On the other hand, direct numerical simulations (DNS), as performed for the present study, can be used to identify typical structures in this flow and to extract information on their origin without such uncertainties and limitations. In addition, the DNS also provides a database to assess the structure resolving ability of turbulence modelling approaches and to assist in the development of new experimental techniques for structure identification.

Even though there is a consensus in the literature on the existence of coherent structures, a clear definition is still elusive. For the present investigation of wake flows, we follow Robinson [14] who, in his review on coherent motions in the turbulent boundary layer, classifies turbulent coherent structures predominantly as shear layers or 'vortices.' Unfortunately, the definition for a vortex is as elusive as the one for a coherent structure and the statement is frequently made that there are as many definitions as researchers in the subject. Robinson [14] defines a *vortex* as a region where 'instantaneous streamlines mapped onto a plane normal to the vortex core exhibit roughly circular or spiral pattern, when viewed from a reference frame moving with the centre of the vortex core.' This definition seems intuitively appropriate, however its usefulness is severely limited by the fact that neither streamlines nor velocity vectors are Galilean invariant, and, consequently, this definition requires an a priori knowledge about the location and convection speed of the vortex. Finding an appropriate reference-frame velocity will be cumbersome at the very least. A more practical definition is given by Chong *et al.* [15]. They define a *vortex core* as 'a region of space where the vorticity is sufficiently strong to cause the rate-of-strain tensor to be dominated by the rotation tensor.' This definition allows the use of criteria based on invariants of the velocity gradient tensor, thus being Galilean invariant. It is adopted in the following as the definition for a *vortical structure*. The term *coherent structure* then includes vortical structures and shear layers. We will call coherent structures 'large' if their extent, in at least one dimension, is of the order of or larger than a characteristic length-scale, say the body height or the shear-layer thickness. Presumably, these structures then confine a flow area with a significant amount of kinetic energy, momentum and/or enstrophy.

The aim of the present study is to identify typical coherent structures in supersonic axisymmetric wakes. Eduction of coherent (or vortical) structures from a given flow field requires an identification technique. In the literature, a host of methods has been proposed, albeit analyses and tests have al-

most exclusively been performed for incompressible flows. What kind of structures these methods can reliably identify in supersonic axisymmetric wakes is therefore still unclear and will be investigated in the present paper. In Section 2 a general discussion of various methods is presented. Methods deemed practical for the present investigation are described in greater detail and the impact of compressibility on generation and identification of coherent structures is addressed. Furthermore, a measure for assessing the reliability of the so-called Q-criterion for compressible flow is proposed (for the corresponding analysis see Appendix A). The methods of choice are applied to three-dimensional data of axisymmetric wakes obtained using DNS to avoid any uncertainties due to the modelling of turbulence. Governing equations, numerical method and simulation parameters are briefly described in Section 3. In Section 4.1, information available in the literature is reproduced to demonstrate the state-of-the-art in structure identification for wake flows and to provide information on what kind of structures can be expected. For reference, results of a three-dimensional plane wake simulation are presented in Appendix B. In Section 4.2, full three-dimensional eduction of coherent structures in the supersonic axisymmetric wake is performed. Thereby the limitations of various visualisation techniques and their reliability are discussed. In Section 4.3, the wake is excited by introducing small perturbations into the shear-layer. The combination of such forced flow simulations with statistical and visualisation techniques for coherent structure identification is used to gain further evidence for the existence of typical structures found in Section 4.2 and to improve their 'visibility.' Section 5 concludes the discussion with a summary of the most important results.

2 Identification techniques

Coherent structure identification methods can be classified in two categories: i) flow visualisation techniques, and ii) statistical methods. Visualisation techniques use instantaneous quantities, of the flow field to reveal the presence of specific structures. On the other hand, statistical methods can be considered as a decomposition of the flow field in components corresponding to extracted structures and leftovers. In the following overview, the formulae used for coherent structure identification in Section 4 are boxed for emphasis.

2.1 Visualisation techniques

2.1.1 Closed streamlines in a coordinate system moving with the structure

This criterion is essentially the definition of a 'vortex' by Robinson [14] as quoted in the introduction. The direct application of this definition requires a priori knowledge of the convection speed of the structures under investigation. For simple, two-dimensional flows, it can be sufficient to subtract the time-averaged flow field and look at instantaneous streamlines or, equivalently, velocity vectors of the disturbance velocity field. Unfortunately, in three-dimensional flows, as illustrated in [16], streamlines in a plane can lead to misinterpretations of vortical structures unless the plane is a plane of symmetry. Hence this method is unattractive for eduction of vortical structures in turbulent flows.

2.1.2 Vorticity

It is understood that a vortical structure must possess vorticity. Therefore, it seems natural to look at instantaneous contours of vorticity magnitude or vorticity components. Unfortunately, the highest levels of vorticity are usually found in shear layers and close to walls where velocity gradients of the mean flow are high. Hence, instantaneous layers of high shear, mean flow gradients and vortical structures can not be distinguished. In addition, if a vortical structure is not aligned with a coordinate axis, contours of vorticity components will yield a misleading picture of the structure. However, if the structure is approximately aligned with a coordinate axis, then the sign of an appropriate vorticity component can serve to indicate the sense of rotation.

2.1.3 Local pressure minimum

The idea of looking at local pressure minima is derived from a simple balance of centrifugal and pressure forces for an inviscid fluid in rotation. Plotting instantaneous iso-surfaces or contours of pressure will then reveal closed contours in the vicinity of the local minimum. This is a straight forward method, but the results can be misleading as discussed in [17]. Nevertheless, for turbulent flows, plotting contours of pressure disturbances is often reported in the literature to visualise large coherent structures more clearly than alternative methods (see [18], for example).

2.1.4 Analysis of the velocity-gradient tensor for vortex core identification

Methods based on this analysis are closely related to finding the eigenvalues of the velocity-gradient tensor $\partial u_i/\partial x_j = \nabla \mathbf{u}$. These eigenvalues λ can be found by solving the characteristic equation,

$$\lambda^3 + P\lambda^2 + Q\lambda + R = 0\,. \tag{1}$$

P, Q and R are the (principal) invariants of $\nabla \mathbf{u}$,

$$P = -\frac{\partial u_i}{\partial x_i}\,, \tag{2}$$

$$\boxed{Q = \tfrac{1}{2}\left(P^2 + W_{ij}W_{ij} - S_{ij}S_{ij}\right)}, \tag{3}$$

$$R = -\mathrm{Det}\left[\frac{\partial u_i}{\partial x_j}\right]\,, \tag{4}$$

with the strain-rate and vorticity tensors

$$S_{ij} = \frac{1}{2}\left(\frac{\partial u_i}{\partial x_j} + \frac{\partial u_j}{\partial x_i}\right)\,, \tag{5}$$

$$W_{ij} = \frac{1}{2}\left(\frac{\partial u_i}{\partial x_j} - \frac{\partial u_j}{\partial x_i}\right)\,, \tag{6}$$

being the symmetric and antisymmetric part of $\nabla \mathbf{u}$, respectively. It should be noted that methods based on (scalar) invariants or eigenvalues of the velocity gradient tensor are Galilean invariant and thus independent of the velocity of the reference frame. In addition, all invariant-based methods are local criteria in the sense that only the velocity gradient tensor at a given point within the flow field needs to be known in order to determine whether the same point is within a vortical structure or

not. However, the use of scalar quantities alone cannot give information on the sense of rotation of a vortical structure. The most popular methods are the Δ, Q, λ_2, and swirling strength criteria, which will be discussed below. It should be noted that, except for very special cases, these methods yield very similar results for incompressible flow, see [17], [19], or [20], for example. The analysis of the relationship between these methods by Chakraborty *et al.* [20] even suggests the possibility of an 'equivalent threshold' for most incompressible flows.

The Δ-*criterion* (cf. Chong *et al.* [15]) is based on a critical point analysis of the velocity gradient tensor. Circular instantaneous streamlines around a point in a coordinate system moving with the velocity of this point can be expected for complex eigenvalues of $\nabla\mathbf{u}$. This is the case if

$$\boxed{\Delta_C = 27R^2 + \left(4P^3 - 18PQ\right)R + \left(4Q^3 - P^2Q^2\right) > 0}\,. \tag{7}$$

For incompressible flow, $P = 0$ due to continuity, then this criterion simplifies to

$$\Delta = (Q/3)^3 + (R/2)^2 > 0\,. \tag{8}$$

Thus $\Delta_C > 0$ or $\Delta > 0$ identifies vortical structures in the sense of the definition of Robinson [14].

The Q-*criterion* (cf. Hunt *et al.* [21], Dubief & Delcayre [19]) is named after the second invariant of $\nabla\mathbf{u}$. For incompressible flow, Q simplifies to

$$\boxed{Q = \tfrac{1}{2}\left(W_{ij}W_{ij} - S_{ij}S_{ij}\right) = \tfrac{1}{4}\left(\Omega^2 - S^2\right)}\,. \tag{9}$$

This can be interpreted as a balance between the squares of the magnitudes of rotation, Ω^2, and strain, S^2. For $Q > 0$,[1] rotation dominates straining, thus fulfilling the definition of vortical structures given in Section 1, i.e. the definition of Chong *et al.* [15]. By inspecting (8), we see that for $Q > 0$ follows $\Delta > 0$. Consequently, for incompressible flow, the criterion of positive Q is more strict than the Δ-criterion and, hence, the definition of Chong *et al.* [15] is more strict than the one of Robinson [14].

According to Jeong & Hussain [17], a further improvement in predicting the presence of vortical structures can be achieved if one considers the eigenvalues for $\Lambda_{ij} = S_{ik}S_{kj} + W_{ik}W_{kj}$ instead of those of $\nabla\mathbf{u}$. Note that all eigenvalues are real, because Λ_{ij} is a symmetric tensor. For at least two negative eigenvalues, domination of rotation over straining is ensured if effects due to viscous diffusion, irrotational straining and compressibility are discarded. This method is called the λ_2-*criterion* when negative contours of the second largest eigenvalue λ_2 are examined. Note that the assumption of incompressible flow is inherent to the derivation of this criterion in order to gain any of the potential improvements over the Q-criterion reported in [17]. For compressible flow, there is no reason for these improvements to hold.

The *swirling strength criterion* (Zhou *et al.* [22]) is closely related to the Δ criterion. For $\Delta > 0$, two eigenvalues of the velocity gradient tensor form a complex conjugate pair, $\lambda_{cr} \pm i\,\lambda_{ci}$, where the magnitude of the imaginary part determines the rate of the swirling motion around the vortex centre and therefore is a measure for the swirling strength. The sign of the real part determines whether the

[1] Hunt *et al.* [21] define the invariant as $II = -Q$, thus $II < 0$. In addition, they employ this criterion in conjunction with a local pressure-minimum condition.

motion of a fluid particle is outward or inward spiralling, i.e. whether coherence of the vortical structure is decreased or increased, respectively. Zhou *et al.* [22] proposed to plot contours of λ_{ci}^2 and employed this method to visualise so-called hairpin vortices in channel flow. Chakraborty *et al.* [20] observed that using small positive thresholds for λ_{ci} and Δ may yield very different results. In addition, they noted that for sufficiently large positive values of λ_{cr}, fluid particles are spiralling outward so rapidly that a vortical structure would lack any coherence whereas both the swirling strength and the Δ criterion still predict the existence of a vortex core. To alleviate this problem, Chakraborty *et al.* [20] suggest to augment the swirling strength criterion by plotting contours λ_{ci} with the additional constraint of $r = \lambda_{cr}/\lambda_{ci} \leq \delta$ with δ being a positive threshold value. They termed the ratio r '*inverse spiralling compactness*' since negative and small positive values of this ratio ensure that orbits of material points around the axis of rotation will remain compact. They also showed that, for incompressible flow, admissible values of the inverse spiralling compactness for the Q and λ_2 criteria are automatically bounded by $-1/\sqrt{3} < r < 1/\sqrt{3}$ for $Q > 0$ and $-\delta < r < \delta$ for $\lambda_2 < 0$ with δ being a flow-dependent parameter of the order of one. These inherent bounds confirm again that $Q > 0$ and $\lambda_2 < 0$ are more strict criteria than $\Delta > 0$.

The above methods are Galilean invariant, but they are not invariant with respect to rotation of the reference frame. The Q-criterion can be corrected in a straight forward manner by subtracting the rotation rate from the vorticity tensor. But according to Haller [23], this is only sufficient in two dimensions. For three-dimensional flows, he proposes instead an 'objective criterion' which includes the time-derivative of the strain-rate tensor.

2.1.5 Shear-layer visualisation using the second invariant of the strain-rate tensor

This method was proposed by Meyer [24]. The second invariant of the strain-rate tensor, S_{ij}, can be written as

$$II_S = \frac{1}{2}\left(S_{ii}S_{jj} - S_{ij}S_{ij}\right) . \tag{10}$$

The use of the invariant ensures a measure of the magnitude of strain independent of the coordinate system. It can be seen as a balance between shearing and stretching. For $II_S < 0$, shearing is stronger than stretching. In [24] the usefulness of this method is demonstrated for a transitional boundary-layer. In this study, negative II_S contours highlighted regions of high shear in the presence of so-called Λ-vortices.

2.2 Statistical methods

2.2.1 Conditional sampling

These methods are frequently used for experimental investigations. A priori knowledge of some characteristics of the structure to be detected is required in order to obtain a condition to base the sampling upon. Only structures with this characteristic will then be identified, other structures might go along undetected. This biases the outcome toward the 'prejudices' of the observer. The *variable interval time-averaging* (VITA) method is arguably the most popular method in the literature. For this method, a

coherent event is deduced if the local variance of the measured signal (to a running or a short-time average) attains a predetermined level. Other methods use local gradients, high-frequency intermittency, the sign (quadrant) of the product of two velocity components, etc. A review on conditional sampling techniques can be found in [25]. Yuan *et al.* [26] compared various methods for a turbulent boundary layer with zero pressure gradient. Not surprisingly, they found that different conditions deduced the presence of different coherent structures. From inspecting the literature, these conditional sampling methods seem less promising for the present study and, consequently, are discarded.

A method strongly related to conditional sampling is the *linear stochastic estimation* (LSE, cf. [27, 28]). In LSE, an estimate for a conditional probability density function (CPDF) is obtained by sampling with respect to a reference signal. Symbolically, we may write

$$\hat{\phi}(x_i, t) = a_j(x_i)\, \varphi_j(t)\,, \tag{11}$$

where ϕ and φ can be any flow variable, $\hat{\phi}$ is the linear estimate of the CPDF of ϕ, and the φ_j are the N known points of the reference signal. $a_j(x_i)$ is the solution of the N equations

$$\langle\, \phi(x_i, t)\, \varphi_k(t)\, \rangle = a_j(x_i)\, \langle\, \varphi_j(t)\, \varphi_k(t)\, \rangle\ , \tag{12}$$

with $\langle\cdot\rangle$ denoting an average in time t. This leads to a linear estimate of the contribution of the reference signal to the average. The method seems especially promising if the flow is forced and the forcing signal is known.

2.2.2 Decomposition techniques

These methods are essentially 'structure filtering' techniques. The flow field is triple decomposed, in an average, a part associated with the coherent structures, and random noise. Most methods are based on Fourier transforms, e.g. *band-pass/band-reject filters* (for examples see the review of Bonnet & Delville [28]) and decomposition of the flow field based upon a *wavelet analysis* ([29, 30]).

The most popular method by far is the use of *proper orthogonal decomposition* (POD, cf. [27]). The POD extracts a basis for a modal decomposition of the flow field by finding eigenvalues and eigenfunctions of the two-point correlation tensor. The basis is optimal in the sense that this decomposition requires the least modes in order to capture the most kinetic energy contained in the flow. Assuming that the most relevant structures in the flow contain the most kinetic energy, then POD seems to be an ideal tool to extract exactly these structures. The algorithm applied for the present study follows [31]: the two-point auto-correlation tensor is given as

$$r_{ij}(x_k, y_k) = \langle\, u_i(x_k, t)\, u_j(y_k, t)\, \rangle\,. \tag{13}$$

Again we take $\langle\cdot\rangle$ as a time average. The eigenvalues λ and eigenfunctions $\sigma_j(x_k)$ can then be found as solutions to the Fredholm integral equation of the second kind over the volume V

$$\boxed{\int_V r_{ij}(x_k, y_k)\, \sigma_j(y_k)\, \mathrm{d}V = \lambda\, \sigma_i(x_k)}\,. \tag{14}$$

In order to save computational effort, the *method of strobes* (or method of snapshots) as introduced in [32] is then used for the actual computation. The eigenfunctions are orthogonal and can be normalised.

Furthermore, the kinetic energy contained in POD mode n is equal to $1/2\ \lambda^2_{(n)}$, thus the most energetic structures are easily identified. Note that for a travelling structure two independent modes are necessary to capture it completely, e.g. a travelling wave has a cosine and a sine component in order to describe all phase locations of the wave. In POD, the eigenvalues of the two modes will have roughly equal values, since the energy content of the structure is largely unaffected from the relative phase location. Note also that using the vorticity vector instead of the velocity vector in (13) results in a decomposition optimal with respect to enstrophy.

Great care has to be taken when attempting to identify or to assess the importance of structures using POD alone. The reason for this is that each POD-mode individually may differ from any of the flow structures which could be considered as 'typical,' e.g. those identified using the various visualisation techniques discussed in Section 2.1. This was demonstrated in [33] for a two-dimensional von Kármán vortex street behind a bluff body. In this study, the flow field analysis using proper orthogonal decomposition showed that the von Kármán vortex street is sufficiently represented by a superposition of only three pairs of POD-modes (in addition to the mode capturing the mean flow). Each pair was attributed to a distinct peak in the temporal spectrum. However, the energy distribution among mode pairs was quite disparate. The higher (less energetic) POD-modes are needed to 'move' and 'stretch' the more generic structure of the dominant mode pair to the 'appropriate' place and shape. If the less energetic modes were discarded, then the typical features of a von Kármán vortex street would not be recovered.

2.2.3 Pattern recognition methods

The combination of spatial correlations, POD-modes or any other 'pattern' with conditional sampling leads to pattern recognition methods. These methods are popular with experimentalists, very likely because many promising alternative methods often require the taking of derivatives of measured quantities, which, in most experiments, is difficult and leads to noisy signals. See [34] for a pattern recognition algorithm applied to a turbulent cylinder-wake, for example.

2.3 Influence of compressibility

Compressibility, i.e. the possibility of density gradients in space and time, introduces further complications with respect to coherent structure identification. One reason is the generation of new kind of structures, such as shocks, shocklets, expansion fans and acoustic and entropy waves. These additional structures require identification criteria or at least 'visualisation tools,' such as Schlieren or Mie-scattering techniques in experiments (see [35] and [36], respectively) or, more conveniently for analysing DNS data, plotting contours of density gradients, dilatation or local Mach number, to name only a few.

In addition to different types of flow structures, compressibility is also responsible for additional hydrodynamic instability mechanisms leading to the formation of coherent structures. One such mechanism is the *baroclinic torque* which can generate vortical structures due to the misalignment of pressure and density gradients. Another mechanism is a hydrodynamic instability due to a 'generalised inflection

point' in the velocity profile (see the review of Mack [37]) which causes vorticity waves to grow.

Furthermore, some techniques used for incompressible flows might be compromised in their performance and require compressible extensions. Rowley *et al.* [38] suggest that, for POD, the vector $u_i(x_k, t)$ in (13) should contain an additional component representing the thermodynamic variables. The term is included to guarantee optimal decomposition of total energy rather than kinetic energy alone, hence taking into account the importance of thermodynamic variables for compressible flows. Also the second invariant of the velocity-gradient tensor Q contains the dilatation P which will show shocklets in addition to vortical structures. Similarly, pressure contours will overlap vortices with shocks. Both methods do not have the ability to separate these structures, thus loosing clarity in representing vortical structures. However, since any combination of the principal invariants leads to another invariant, we can subtract P^2 from the definition of the second invariant in (3). The result is the incompressible form of Q, i.e. (9). Thus using (9) to identify vortical structures might still be viable, since it maintains its original meaning of a balance of rotation and strain while still being Galilean invariant. On the other hand, the λ_2-criterion inherently assumes incompressibility in its derivation in order to obtain any advantage it might have over the Q criterion and, consequently, these advantages can not be guaranteed for compressible flow whereas a generalisation of this criterion is not obvious.

Further insight into the applicability of identification techniques based on invariants of the velocity gradient tensor to compressible flows can be gained by generalising the analysis of Chakraborty *et al.* [20] with respect to inherent bounds of inverse spiralling compactness. Such an analysis is performed for the Q-criterion in Appendix A. It shows that, in general, $Q > 0$ obeys bounds on $r = \lambda_{cr}/\lambda_{ci}$. However, for compressible flow, these bounds are flow dependent and might even vary within the flow field. If the upper bound moves too far towards positive values then swirling motion with little coherence will be wrongly identified as a vortex core. Conversely, if the upper bound reaches too low values, e.g. negative values of r, then some vortical structures are likely to be not detected. On the other hand, the incompressible form of Q applied to compressible flow maintains bounds of the order of one, however, the range of admissible values of $\lambda_{cr}/\lambda_{ci}$ narrows and might even vanish, i.e. this criterion becomes stricter with increased compressibility of the flow. Critical for the applicability of either criterion to compressible flow is that the magnitude of the parameter

$$a = P/(3\,\lambda_{ci}) = -\frac{\partial u_i}{\partial x_i}/(3\,\lambda_{ci}) \tag{15}$$

remains small (see the analysis in Appendix A). This parameter could be regarded as a measure for the impact of compressibility on a vortex core and as such will be termed *vortex compressibility parameter* in the following. It represents a ratio of the local rate of compression or expansion (depending on the sign) over the local swirling rate λ_{ci}. Or in other words, for $a \to 0$, the swirling motion is much faster than the time-scales required for compression or expansion such that these effects can be neglected when identifying a vortical structure. Instead of computing the vortex compressibility parameter, it is possible to apply the general and the incompressible form of Q to the same data set. This approach is followed in Section 4.2. If, using the same threshold value, both methods predict the presence of structures of similar shape, size and strength then the parameter a will be sufficiently small for

either method to be reliable. Such a conclusion is possible since increasing the magnitudes of the vortex compressibility parameter affects both methods in very different ways (again see Appendix A). Nevertheless, great care has to be taken when employing these criteria to identify vortical structures in compressible flows.

3 Computational setup

3.1 Governing equations

The compressible Navier–Stokes equations form the set of governing equations. The (dimensionless) equations solved are the continuity equation

$$\frac{\partial \rho}{\partial t} + \frac{\partial}{\partial x_j}\left(\rho u_j\right) = 0\,, \tag{16}$$

the momentum equation

$$\frac{\partial \rho u_i}{\partial t} + \frac{\partial}{\partial x_j}\left(\rho u_i u_j + \delta_{ij} p - \tau_{ij}\right) = 0\,, \tag{17}$$

and the energy equation

$$\frac{\partial E}{\partial t} + \frac{\partial}{\partial x_j}\left([E+p]u_j - u_i\tau_{ij} + q_j\right) = 0\,. \tag{18}$$

u_i is the velocity vector, ρ the density, T the temperature, and p the pressure. The viscous stress, energy, and heat flux are

$$\tau_{ij} = \frac{2\mu}{Re}\left(S_{ij} - \frac{1}{3}\delta_{ij}S_{kk}\right)\,, \tag{19}$$

$$E = \rho\left(\frac{T}{\gamma(\gamma-1)Ma^2} + \frac{u_k u_k}{2}\right)\,, \tag{20}$$

$$q_i = -\frac{\mu}{(\gamma-1)Ma^2 RePr}\frac{\partial T}{\partial x_i}\,, \tag{21}$$

respectively. The viscosity μ is computed applying Sutherland's law (cf. [39]); $\gamma = 1.4$ and Prandtl number $Pr = 0.71$. Mach number Ma and Reynolds number Re are constants as specified for the case investigated and the strain-rate tensor S_{ij} is given by (5). Furthermore, we invoke the equation of state for a perfect gas to determine the pressure

$$p = \frac{\rho T}{\gamma Ma^2}\,. \tag{22}$$

In Section 4.3, the supersonic axisymmetric wake is perturbed by adding a time-dependent volume force in Fourier space to the right-hand-side of the radial momentum equation (17):

$$F^k = A_{dist}\sin(2\pi f t)\left[1-\cos\left(\frac{(r-r_b)\pi}{r_e-r_b}\right)\right]\left[1-\cos\left(\frac{(z-z_b)\pi}{z_e-z_b}\right)\right]\,, \tag{23}$$

with k denoting which azimuthal Fourier mode is forced, and r_b, r_e, z_b and z_e being the starting and end points of the forcing in the radial and the streamwise directions, respectively. The forcing amplitude for all cases discussed in this paper was fixed to $A_{dist} = 1.0$ and the frequency, f, was set to zero for steady forcing or given a specified value for time-periodic forcing. To solve the above equations, boundary and initial conditions must be supplied. These are described in detail in [40].

3.2 Numerical method

For the results presented in this paper, a flow solver based on a cylindrical coordinate system was employed for integrating the governing equations. The solver uses the standard fourth-order Runge–Kutta scheme for time-advancement and high-order accurate split finite-differences in the spatial directions within a two-dimensional plane, i.e. sixth-order accurate compact differences and fourth-order accurate differences in the radial and downstream directions, respectively. To allow for grid-stretching while preserving accuracy, all finite differences are derived for non-equidistant grids. Wall boundary conditions are implemented with high-order accuracy (fourth or fifth). A pseudo-spectral discretisation is used in the azimuthal direction, thus enabling a state-of-the-art axis treatment exploiting parity conditions in Fourier space (cf. [40]). An additional feature of the solver is an efficient parallelisation using a domain decomposition technique.

3.3 Simulation parameters

Axisymmetric wakes at a Mach number of $Ma = 2.46$ and a range of Reynolds numbers ($30,000 \leq Re_D \leq 100,000$) were computed with results being presented for the lowest and highest Reynolds number only. All quantities were made dimensionless using the radius R of the bluff body and reference quantities at the corner of inflow and free-stream boundaries. At the inflow a compressible similarity solution was specified such that for all cases, the boundary layer thickness at the separation point was $\delta = 0.1$. Using symmetric Fourier transforms in the azimuthal direction, the circumferential extent of the computational domain was $0 \leq \theta \leq \pi$. In the streamwise/radial plane, the domain size of the DNS at $Re_D = 3 \times 10^4$ was $-1.0 \leq z \leq 12$ and $0 \leq r \leq 6$ with the origin of the coordinate system at the centre of the base. The flow was dicretised using a stretched grid with 452×130 points in the z- and r-directions, respectively, and 32 Fourier modes in the azimuthal direction. At $Re_D = 10^5$, the computational domain ranged from $-1.0 \leq z \leq 15$ and $0 \leq r \leq 6$ and was discretised with 1272×160 points in the streamwise and radial directions, respectively. At this higher Reynolds number, 129 Fourier modes were employed. The timestep was determined by globally satisfying the diffusion and CFL limits. This resulted in $\Delta t = 1.5 \times 10^{-3}$ and $\Delta t = 8 \times 10^{-4}$, for $Re_D = 3 \times 10^4$ and $Re_D = 10^5$, respectively. Further details on the simulations, resolution studies and mean flow results (not presented here) are given in [40].

4 Results

4.1 What kind of structures can we expect?

In the literature, much is known about coherent structures and their formation in incompressible plane wakes (see [41, 42, 43], for example). For plane wakes, beyond a critical Reynolds number a two-dimensional absolute instability creates a von Kármán vortex street with its typical alternating pairs of counter-rotating Kelvin–Helmholtz (KH) vortices. For a sufficiently large Reynolds number, the two-dimensional KH–vortices become unstable with respect to three-dimensional disturbances. Their vortex

cores deform sinusoidally in the lateral direction usually in a varicose fashion. In addition, bundles of thin tubes of high vorticity, frequently called 'braids,' form between the warped KH–vortices. For illustration, results of a three-dimensional simulation of a plane wake at $Re_D = 1,000$ and $Ma = 0.25$ are included in Appendix B showing the KH–vortices and the braids in Fig. 8 and 9, respectively.

For the axisymmetric wakes at the Reynolds numbers presented here, the physical mechanisms leading to the formation of large coherent structures differ from plane wakes. In particular, an absolute instability exists only for helical modes whereas two-dimensional (axisymmetric) waves are only convectively unstable [44]. Therefore, it is reasonable to expect different kind of flow structures for axisymmetric and plane wakes at comparable Reynolds numbers. This is confirmed with the help of Fig. 1 for an axisymmetric wake with $Re_D = 2,000$ and $Ma = 0.25$. The dominant flow structures are visualised using the Q-criterion. Loops of concentrated vorticity are visible which more resemble hairpin vortices in transitional boundary layers than either the KH–vortices or the braids of plane wakes.

To assess the impact of compressibility, the Mach number is increased to 2.46 and also the Reynolds number to $Re_D = 100,000$, since compressibility has a stabilising effect on flow instabilities. The sideview of instantaneous streamwise density-gradient in Fig. 2 shows structures similar to a visualisation using a Schlieren technique of supersonic experiments. Visible flow structures are the expansion fan (white and light grey contours) and the thin shear-layer (black contours) both originating at the corner of the body, shocklets emanating away from the shear-layer and the near wake, and as of yet undefined 'turbulent coherent structures' in the developing wake which will be visualised in more detail in Section 4.2.

For the same Mach number and similar flow conditions (albeit at a higher Reynolds number of $Re_D = 3.3 \times 10^6$), experiments conducted at the University of Illinois at Urbana–Champagne employed a Mie-scattering technique for visualisation of 'large coherent structures.' For this technique, ethanol vapour that is carried in the supply air condenses at flow speeds close to sonic conditions. In order to compare data obtained from DNS with the experimental data, instantaneous, local Mach numbers were chosen for visualisation and the contour levels were adjusted so that the emerging picture resembled that obtained by Bourdon & Dutton [36]. The resulting endviews are compared to the figures obtained from the experiments in figure 3 for streamwise positions that correspond to locations C, D and E in [36].

In spite of the significantly higher Reynolds number investigated experimentally, the resemblance is remarkable. Just upstream of the mean reattachment (here $z = 3.5$), 12 to 14 structures can be detected in the shear layer, in good agreement with the typical number of 10 to 14 observed in the experiments at the same location (C). The streamwise structures appear to undergo an amalgamation in the downstream direction, evidenced by a decreasing number of structures farther downstream. In the developing wake ($z = 6.5$, location E in the experiments), only four main lobes are visible for some instances, as was also the case in the experiments. Furthermore, the mushroom-like shape of the contours, indicating the existence of longitudinal structures, is very similar to the observations in [36].

In summary, due to axisymmetry we can expect hairpin-like vortex loops in the developing wake. For

the shear-layer, stability considerations strongly hint toward helical structures whereas experimental evidence using planar visualisations supports that longitudinal structures might exist as well. In addition, the presence of expansion fans and shocklets suggests that baroclinic torque could be a viable vorticity generation mechanism.

4.2 Three-dimensional identification of coherent structures

Having convinced ourselves that the DNS data at $Re_D = 100,000$ contain flow structures observed in experiments, we use different techniques to visualise the flow field in full three dimensions (Fig. 4). Contour levels of the visualised quantities are selected by scanning through the range of possible values and selecting those which seem to highlight coherent structures best. Plotting instantaneous contours of pressure turns out to be impractical as the expansion fan originating from the base corner conceals most structures present in the near wake. Subtracting the mean flow removes the (steady) expansion fan and only the time-dependent fine-scale structures remain visible. The visualisation of pressure disturbances in Fig. 4 reveals structures only in the developing wake region. Reducing the contour level of disturbance pressure anticipating that coherent structures in the shear layer would be highlighted leads to a large number of structures in the free-stream obscuring the view of the near wake. These structures most likely represent acoustic waves radiating into the far field. It therefore appears that contours of instantaneous pressure fail to visualise helical and longitudinal structures in the shear layer (seen when employing other visualisation techniques). Thus this method does not seem to be suited for the visualisation of coherent structures in supersonic axisymmetric wakes. Note that the requirement of a converged mean pressure field can also make this method computationally expensive when employing DNS.

The visualisation of vorticity magnitude shows sheets of high vorticity in the shear layer, resembling longitudinal vortices upstream of the recompression region. These structures most likely are responsible for the mushroom-shaped contours observed in the endviews (Fig. 3). Note, that these vortices are not introduced by forcing as in the cases presented in Section 4.3, but occur naturally. It appears that the longitudinal structures do not persist throughout the recompression region. Instead, they seem to break up, forming a considerable number of small scale vortex loops downstream of the recompression region. These hairpin-like vortex loops can also be identified with any of the invariant-based methods (Δ_C, Q, and Q^*) with Q^*, the incompressible form of Q, showing them most clearly. The methods differ, however, in the structures extracted from the shear-layer. The compressible Δ-criterion focusses on longitudinal structures, whereas the compressible and incompressible definitions of Q highlight helical structures in the shear layer.

According to the reasoning in Section 2.3, the reliability of the Q-criterion and its incompressible form is high since both methods reveal the same kind of flow structures. In addition, helical structures are consistent with stability considerations of an axisymmetric supersonic base–flow [44]. That these criteria do not show the longitudinal structures in sufficient clarity could have three reasons: (1) These structures do not exist, but are wrongly shown using other methods. However, longitudinal structures were (indirectly) observed in the experiments (see Section 4.1). (2) Since Q is a 'strict criterion'

(compared to Δ_C), it might miss some vortical structures, in particular, if these undergo rapid axial straining and, as a consequence, the lower bound of the inverse spiralling compactness observed by this criterion (see Appendix A) is not reached. (3) The longitudinal structures are merely hidden by overlapping contours of other structures. If the latter is true, then 'emphasising' the longitudinal structures, i.e. altering their strength by artificial excitation, will change the appropriate contour level and, hence, alleviate this problem. That this is indeed the case is shown in Section 4.3 albeit for a lower Reynolds number. A possible explanation for the failure of the Δ_C-criterion in educing the helical structures is that contour levels required for their visualisation are likely to be very small. Using the incompressible comparable threshold proposed in [20] as a guideline, an equivalent contour level for Δ_C can be estimated from the threshold used for the Q-criterion as $\varepsilon_\Delta = O(\varepsilon_Q^3) = 10^{-3}$. For such a small threshold (if it were to be the appropriate one), it is common for Δ_C to wrongly identify other kind of flow structures as vortex cores and their contours would then superimpose with those of the helical structures obstructing the view. Note that contours of Q of the order of 10^{-1} were also suitable for the incompressible axisymmetric wakes (see Fig. 1, for example) and are therefore rather a consequence of axisymmetry than compressibility of the flow. This is corroborated by the one order of magnitude larger values required for highlighting the coherent structures in the plane wake example in Appendix B.

As was discussed in Section 2.3, baroclinic torque is an inherently compressible mechanism to generate vorticity. This suggests that this quantity might also be used as a diagnostic tool for identifying coherent structures. Scrutinising contours of the magnitude of baroclinic torque, shown in Fig. 4, it can be observed that a significant amount of vorticity generation occurs in the shear layer. In fact the structures visualised using this technique resemble the helical structures found in the shear layer employing contours of Q (this can be seen more clearly for lower Reynolds numbers). Just downstream of separation, it appears as if 'patches' with a regular azimuthal spacing are present, thus (indirectly) indicating the existence of longitudinal structures. In the developing wake, a large amount of hairpin vortices can be observed as with invariant-based methods. It seems that baroclinic torque is a mechanism which enhances or attenuates the most important structures present in supersonic axisymmetric wakes and, hence, plotting contours of the magnitude of baroclinic torque is capable of locating these structures.

4.3 Forcing of the wake

Apart from plotting production terms of the vorticity equation or merely visualising 'naturally' occurring flow structures, the wake can also be perturbed intentionally by introducing (small) artificial disturbances into the shear layer, that is *forcing* the flow. Structures generated in this way can be attenuated or amplified. Amplification of structures is a strong hint that they appear naturally in the investigated flow. In addition, the structures will be more clearly visible and, since the generating perturbations are know, they can also be tracked and analysed with greater ease. For these reasons, educing flow structures by forcing has been successfully applied in the literature for many years, e.g. so-called Λ-vortices in transitional boundary layers in the classical experiments of Klebanoff *et al.* [45]

or coherent structures in the fully turbulent plane wake experiments of Wygnanski *et al.* [3].

Forcing of the supersonic axisymmetric wake was carried out for Reynolds numbers in the range of $3 \times 10^4 \leq Re_D \leq 3.3 \times 10^6$ (using a large eddy simulation turbulence modelling approach for the highest Reynolds numbers). The increase in Reynolds number had an impact on the growth rates of amplified structures, but the principle of forcing as a diagnostic tool was successful nevertheless. The forcing is accomplished by introducing perturbation into the approach boundary layer, just upstream of separation with the centre of the disturbances at $r = 1.05$ and $z = -0.15$, through a time-periodic volume force F^k as given in Section 3.1. The volume force was added to the right-hand-side of the radial momentum equation in Fourier space, thus a specific azimuthal mode k could be forced.

In Fig. 5, instantaneous contours of Q are employed to show vortical structures in the axisymmetric wake at a lower Reynolds number of $Re_D = 30,000$ than the simulation results from above, but otherwise identical conditions. The unforced flow (left) is shown for reference. It exhibits the same kind of helical structures in the shear layer as the flow at the higher Reynolds number discussed above. However, there is a delay in formation of the vortex loops (hairpins) which appear to be larger in size and possess longer and more clearly visible 'legs.' These legs are actually thin tubes of concentrated longitudinal vorticity which emanate from the region of recirculating flow and are stretched in the developing wake until they roll up to become hairpins. Introducing steady longitudinal vortices into the shear layer by forcing the azimuthal mode $k = 16$ (Fig. 5, right) obstructs the helical structures and sheets of longitudinal vorticity become evident. In addition, the roll up of the longitudinal vortical structures in the developing wake occurs farther upstream. On the other hand, forcing mode $k = 4$ (not shown) shows little difference to the unforced case, hence suggesting that longitudinal structures with this azimuthal spacing are not supported within the shear-layer. Time-dependent, axisymmetric ($k = 0$) forcing of the shear-layer with a Strouhal number of $St = 0.83$ (Fig. 6, top left) emphasises helical structures in the shear layer with the same frequency and the roll up to hairpins is accelerated as well.

Finally, the (forced) flow is decomposed using POD. The case with time-dependent axisymmetric forcing was selected because the dominant structures could be associated with the forcing frequency, hence determining the temporal resolution required for the POD. Forcing the flow with $St = 0.83$, two data sets were analysed, one with a sampling time of $t = 4/St = 4.82$ and a sampling rate of $\Delta t = 0.03$ and the other with $t = 20/St = 24.10$ and $\Delta t = 0.15$. Because both analyses with the POD yielded similar results for the eigenfunctions, only the results of the analysis of four forcing periods are discussed in the following.

The zeroth POD-mode is virtually identical to the mean flow and contains by far the most kinetic energy. In Fig. 6, the top left plot shows the original flow field, whereas in the top right plot the first 32 POD-modes are used to approximate the flow field. The helical structures in the shear layer and the hairpins in the developing wake are represented by these POD-modes in a generic manner. The travelling structures in the shear layer appear in pairs. The first (and most energetic) of these modes is shown on the bottom left. The helical structure is more clearly visible and seems to reach farther downstream than in the original flow field since it is not obstructed by superposition with other

structures demonstrating the ability of POD to serve as a structure filter. However, as was pointed out in Section 2.2.2, a single POD-mode is not necessarily a typical flow structure by itself. This can be seen by the inclusion of the thin longitudinal 'legs' in the developing wake of the dominant mode. On the other hand, the hairpin structures do not belong to this mode, they only become visible by addition of several higher modes (bottom right). These modes of lesser energy contents are necessary to deform and 'move' the 'legs' in the developing wake such that they resemble 'typical structures' extracted with visualisation techniques. However, contrary to the plane wake example cited in Section 2.2.2, the energy contained in these higher modes is not insignificant with the second and third pair containing 31% and 16% of the energy of the first pair, respectively. Nevertheless, an important fact that can be determined from the POD analysis is that the structures containing most kinetic energy are helical within the shear layer and longitudinal vortex tubes in the developing wake, whereas the hairpin-like structures contain only a smaller amount of kinetic energy.

5 Conclusions

Direct numerical simulation data of supersonic axisymmetric wakes behind bluff bodies were analysed for the existence of large coherent structures. Criteria for identification of coherent structures in free-shear flows found in the literature were compiled and discussed. In addition, the role of compressibility was addressed and for the Q-criterion analysed in greater detail. The identification methods deemed most practical for the present investigation were applied to the full three-dimensional data sets for $Ma = 2.46$ and $30,000 \leq Re_D \leq 100,000$ with results being presented for the lowest and highest Reynolds numbers only.

Employing the Q-criterion to visualise DNS data of an axisymmetric wake at $M = 0.25$ illustrated that the large coherent structures differ significantly from the plane wake. To investigate the effect of compressibility, DNS of supersonic wakes were conducted with an emphasis on a case at $Re_D = 100,000$ and $Ma = 2.46$. The similarity of the numerical simulations with experiments was established by using planar visualisations of contours of Mach number. Various visualisation techniques were then employed to obtain a three-dimensional picture of the supersonic axisymmetric wake which in this detail to-date has not been obtained using neither experiments nor simulations. The use of velocity-gradient based visualisation techniques revealed the existence of longitudinal and helical structures in the initial shear layer, and a large number of hairpin structures in the developing wake. At lower Reynolds numbers, elongated tubes of streamwise vorticity are observed to emanate from the region of recirculating flow and to evolve into hairpin-like vortex loops in the developing wake.

The present study substantiates the ability of some techniques intended for incompressible shear-flows, e.g. the incompressible form of Q, to educe meaningful structures in compressible wakes if used with care. A low magnitude of the 'vortex compressibility parameter' is proposed as a possible criterion for their applicability. A sufficiently low value is present if the general and incompressible form of the Q-criterion identify the same kind of structures in a given flow field. This was the case in the present study, i.e. identified vortical structures possessed a swirling rate significantly larger than the

rates of compression and expansion present in this flow. On the other hand, employing contours of instantaneous pressure or disturbance pressure failed to visualise the dominant helical and longitudinal structures in the shear layer with sufficient clarity. Thus this method was not suited for the visualisation of coherent structures in the supersonic axisymmetric wakes investigated here. It was further shown that the inherent compressibility effects of supersonic flows can also be exploited for visualisation. Contours of the magnitude of baroclinic torque were shown to be capable of locating the most important structures in compressible turbulent wakes. This in turn shows that the misalignment of pressure and density gradients plays a role in enhancing or attenuating such structures. The usefulness of artificially perturbing (*forcing*) the flow for highlighting coherent structures was demonstrated giving further evidence for the existence of both helical and longitudinal structures within the shear layer. A POD analysis of the flow with axisymmetric, harmonic forcing was conducted. Using the Q-criterion to visualise individual POD-modes revealed that the structures containing most of the kinetic energy are helical within the shear-layer whereas in the developing wake the kinetic energy is concentrated in elongated tubes of longitudinal vorticity and only to a lesser extent in hairpin vortices.

Acknowledgments

The authors are indebted to Professor J. C. Dutton for kindly providing us with pictures from his experiments. Research presented here was supported by the Army Research Office (ARO) under grant number DAAD 19-02-1-0361 #1. Dr. Thomas Doligalski served as program manager. Computer time on the ERDC/HPC under Challenge project VI9ARONC11312C1D is gratefully acknowledged.

A Impact of compressibility on the Q-criterion

The (principal) invariants of the velocity-gradient tensor P, Q and R are uniquely determined by the eigenvalues λ_i $(i = 1, 3)$ of $\nabla\mathbf{u}$:

$$P = -\left(\lambda_1 + \lambda_2 + \lambda_3\right) , \tag{24}$$

$$Q = \lambda_1\lambda_2 + \lambda_1\lambda_3 + \lambda_2\lambda_3 , \tag{25}$$

$$R = -\lambda_1\,\lambda_2\,\lambda_3 . \tag{26}$$

Considering locations in the flow for which holds

$$\Delta_C = 27R^2 + \left(4P^3 - 18PQ\right)R + \left(4Q^3 - P^2Q^2\right) > 0 \tag{27}$$

is equivalent to requiring λ_1 to be real and $\lambda_{2,3} = \lambda_{cr} \pm i\,\lambda_{ci}$ to be complex conjugates, where $\lambda_{ci} > 0$ by definition. Note that, for incompressible flow ($P = 0$), the condition stated in (27) is always satisfied for $Q > 0$, otherwise it poses a necessary constraint on the following analysis.

Introducing the *inverse spiralling compactness* parameter

$$r = \lambda_{cr}/\lambda_{ci} \tag{28}$$

and using (24) to eliminate λ_1 allows us to recast Q in a form depending on r for given P and λ_{ci}:

$$Q = -\left(3\lambda_{ci}^2\right) r^2 - \left(2P\lambda_{ci}\right) r + \lambda_{ci}^2 \,. \tag{29}$$

Normalizing Q with λ_{ci}^2, its maximum value in incompressible flow, yields

$$\widetilde{Q} = Q/\lambda_{ci}^2 = -3\,r^2 - 6\,a\,r + 1\,, \tag{30}$$

where the *vortex compressibility parameter*

$$a = P/\left(3\lambda_{ci}\right) \tag{31}$$

determines the range of r for which positive values of Q can be obtained. For $a \to 0$, the impact of compressibility on the swirling motion is negligible and the flow-independent bounds predicted in [20] for incompressible flow are retrieved:

$$-1/\sqrt{3} < r < 1/\sqrt{3}\,. \tag{32}$$

For non-zero values of a, the region of $Q > 0$ is bounded by

$$-a - \sqrt{a^2 + 1/3} < r < -a + \sqrt{a^2 + 1/3}\,. \tag{33}$$

These are general bounds on the inverse spiralling compactness for vortical structures identified with $Q > 0$ as long as a pair of complex conjugate eigenvalues exists, i.e. (27) holds. For compressible flow, these bounds are flow dependent and are likely to vary within the flow field. In Fig. 7 (left), $\widetilde{Q}$ in dependence on r is shown for selected values of the vortex compressibility parameter. If the magnitude of this parameter increases then the range of r for which $Q > 0$ increases as well, i.e. the method becomes less 'strict.' Moreover, for positive values of this parameter, i.e. negative dilatation, the range of valid r shifts toward smaller values and more and more vortical structures will not be identified as such. For negative values of a, i.e. positive dilatation, the shift is to larger values of r and rapidly outward spiralling fluid motion with little coherence can then be mistaken as part of a vortex core.

The incompressible form of Q (if applied to compressible flow) is equivalent to

$$Q^* = \frac{1}{4}\left(\Omega^2 - S^2\right) = Q - P^2 = -\left(3\lambda_{ci}^2\right) r^2 - \left(2P\lambda_{ci}\right) r + \lambda_{ci}^2 - P^2 \tag{34}$$

or, in its normalized form,

$$\widetilde{Q^*} = Q^*/\lambda_{ci}^2 = -3\,r^2 - 6\,a\,r + 1 - 9\,a^2\,. \tag{35}$$

The inherent bounds on r are

$$-a - \sqrt{1/3 - 2\,a^2} < r < -a + \sqrt{1/3 - 2\,a^2}\,, \tag{36}$$

Note that the magnitude of these bounds will always be smaller than one (see Fig. 7, right) with a maximum of $|r| = 3/\sqrt{18}$ for $a = \pm 1/\sqrt{18}$. However, with increasing compressibility the range of admissible values of r shrinks and vanishes once the magnitude of the vortex compressibility parameter exceeds $1/\sqrt{6}$. Hence, in contradistinction to the compressible form, the criterion $Q^* > 0$ becomes 'stricter' with increased influence of compressibility and, for strongly compressible flows, fails to identify any vortical structures at all.

B Coherent structures in a plane wake

The flow past a two-dimensional bluff body at $Ma = 0.25$ and $Re_D = 1,000$ with a boundary-layer thickness at separation of $\delta \approx 0.2$ was computed using a Cartesian flow solver similar to the cylindrical solver described in Section 3.2 (for details see [33]). For the simulation, all quantities were made dimensionless using the height D of the two-dimensional bluff body and reference quantities at the corner of inflow and free-stream boundaries. The domain size ranged from $-3.0 \leq x \leq 20.67$ and $-3.9 \leq y \leq 3.9$ with the origin of the coordinate system at the centre of the base. At the inflow boundary a Blasius similarity solution with a boundary layer thickness of $\delta \approx 0.2$ was imposed on both sides of the body. The flow was discretised using 190×159 points in the x- and y-directions, respectively. Grid stretching was employed in both directions. Periodic boundary conditions were enforced in the lateral direction and 129 Fourier modes were employed to discretise a domain width of eight body heights. Note that a sufficient spanwise extent of the domain was crucial for inclusion of all possible instabilities of this flow. To this end a lateral domain size and resolution study was carried out which was guided by the findings in [43] for the plane wake behind a circular cylinder at the same Reynolds number. A time step of $\Delta t = 2 \times 10^{-3}$ was used. The simulation time exceeded 30 flow-through times of the computational domain.

In Fig. 8, Kelvin-Helmholtz vortices with strong spanwise deformations are shown using contours of instantaneous total and disturbance pressure. As suggested in Section 2.1.3, pressure contours are indeed able to extract the largest structures for the plane wake at low Mach number. Due to a weakening of the KH–vortices farther downstream, a single iso-contour of disturbance pressure is not able to show all structures in the vortex street, although those shown are captured more concisely than for the case of total pressure. Note that the weakening of the KH–vortices, also possibly physical, is likely to be a numerical artifact of the simulation due to the coarsening of the grid in the downstream direction.

The pressure iso-surfaces failed in educing the braids sufficiently, therefore, they are extracted from the data using the Q-criterion instead (Fig. 9). The braids are strongly lifted up in the y-direction and slightly tilted against the $z = 0$ plane. Hence, they are only approximately aligned with a dominant flow axis, such that these structures can not be clearly identified using vorticity contours. However, by colouring iso-surfaces of Q according to the sign of longitudinal vorticity and of pressure by lateral vorticity, we can indicate the sense of rotation of the braids and the KH–vortices, respectively (not shown here). Inspecting the sense of rotation of the structures, an alternating pattern of clockwise and counter-clockwise rotating spanwise rollers can be seen. This is consistent with a von Kármán vortex street. A similar pattern of pairs of counter-rotating tubes of streamwise vorticity represents the braids. The latter is consistent with the observations in [43].

References

[1] SC Crow and FH Champagne. Orderly structure in jet turbulence. *J. Fluid Mech.*, 48:547–591, 1971.

[2] GL Brown and A Roshko. On density effects and large structure in turbulent mixing layers. *J. Fluid Mech.*, 64:775–816, 1974.

[3] I Wygnanski, F Champagne, and B Marasli. On large-scale structures in 2d small-deficit and turbulent wakes. *J. Fluid Mech.*, 168:31–71, 1986.

[4] S Cannon, F Champagne, and A Glezer. Observations of large-scale structures in wakes behind axisymmetric bodies. *Exps. Fluids*, 14:447–450, 1993.

[5] J Sahu and C Nietubicz. Three-dimensional flow calculations for a projectile with standard and dome bases. *Journal of Spacecraft and Rockets*, 31:103, 1994.

[6] JL Herrin and JC Dutton. Supersonic near-wake afterbody boattailing effects on axisymmetric bodies. *Journal of Spacecraft and Rockets*, 31:1021, 1994.

[7] CJ Bourdon and JC Dutton. Effects of boattailing on the turbulence structure of a compressible base flow. *Journal of Spacecraft and Rockets*, 38(4):534–541, 2001.

[8] J Sivasubramanian, RD Sandberg, DA von Terzi, and HF Fasel. Numerical investigation of flow control mechanisms for drag reduction in supersonic base flows. AIAA Paper 2006–902, 2006.

[9] J Sahu and KR Heavey. Numerical investigation of supersonic base flow with base bleed. *Journal of Spacecraft and Rockets*, 34(1):61–69, 1995.

[10] T Mathur and CJ Dutton. Base-bleed experiments with a cylindrical afterbody in supersonic flow. *Journal of Spacecraft and Rockets*, 33:30, 1996.

[11] T Mathur and CJ Dutton. Velocity and turbulence measurements in a supersonic base flow with mass bleed. *AIAA J.*, 34:1153, 1996.

[12] J Sivasubramanian, RD Sandberg, DA von Terzi, and HF Fasel. Numerical investigation of transitional supersonic base flows with flow control. *Journal of Spacecraft and Rockets*, 44(5):1021–1028, 2007.

[13] RD Sandberg and HF Fasel. Investigation of supersonic wakes using conventional and hybrid turbulence models. *AIAA J.*, 44(9):2071–2083, 2006.

[14] SK Robinson. Coherent motions in the turbulent boundary layer. *Ann. Rev. Fluid Mech.*, 23:601–639, 1991.

[15] MS Chong, AE Perry, and BJ Cantwell. A general classification of three-dimensional flow fields. *Phys. Fluids A*, 2(5):765–777, 1990.

[16] AE Perry and MS Chong. Topology of flow patterns in vortex motions and turbulence. *Appl. Sci. Res.*, 53:357–374, 1994.

[17] J Jeong and F Hussain. On the identification of a vortex. *J. Fluid Mech.*, 285:69–94, 1995.

[18] S Kang and H Choi. Suboptimal feedback control of turbulent flow over a backward-facing step. *J. Fluid Mech.*, 463:201–227, 2002.

[19] Y Dubief and F Delcayre. On coherent-vortex identification in turbulence. *J. Turbulence*, 1:1–22, 2000.

[20] P Chakraborty, S Balachandar, and RJ Adrian. On the relationships of local vortex identification schemes. *J. Fluid Mech.*, 535:189–214, 2005.

[21] JCR Hunt, AA Wray, and P Moin. Eddies, stream, and convergence zones in turbulent flows. In *Proceedings of the 1988 summer conference*. Stanford University, December 1988.

[22] J Zhou, S Balachandar, RJ Adrian, and TM Kendall. Mechanisms for generating coherent packets of hairpin vortices. *J. Fluid Mech.*, 387:353–396, 1999.

[23] G Haller. An objective definition of a vortex. *J. Fluid Mech.*, 525:1–26, 2005.

[24] D Meyer. *Direkte numerische Simulation nichlinearer Transitionsmechanismen in der Strömungsgrenzschicht einer ebenen Platte*. PhD thesis, Universität Stuttgart, 2003.

[25] RA Antonia. Conditional sampling in turbulence measurement. *Ann. Rev. Fluid Mech.*, 13:131–156, 1981.

[26] YM Yuan and MR Mokhtarzadeh-Dehghan. A comparison study of conditional-sampling methods used to detect coherent structures in turbulent boundary layers. *Phys. Fluids*, 6:2038–2057, 1994.

[27] G Berkooz, P Holmes, and JL Lumley. The proper orthogonal decomposition in the analysis of turbulent flows. *Ann. Rev. Fluid Mech.*, 25:539–575, 1993.

[28] J-P Bonnet and J Delville. Review of coherent structures in turbulent free shear flows and their possible influence on computational methods. *Flow, Turbulence and Combustion*, 66:333–353, 2001.

[29] M Farge, G Pellegrino, and K Schneider. Coherent vortex extraction in 3d turbulent flows using orthogonal wavelets. *Phys. Rev. Lett.*, 87(054501):1–4, 2001.

[30] A Rhinoshika and Y Zhou. Orthogonal wavelet multi-resolution analysis of a turbulent cylinder wake. *J. Fluid Mech.*, 524:229–248, 2005.

[31] D Rempfer and HF Fasel. Evolution of three-dimensional coherent structures in a transitional flat-plate boundary layer. *J. Fluid Mech.*, 260:351–375, 1994.

[32] L Sirovich. Turbulence and the dynamics of coherent structures. *Q. Appl. Math.*, 45:561–590, 1987.

[33] DA von Terzi. *Numerical Investigation of Transitional and Turbulent Backward-Facing Step Flows*. PhD thesis, The University of Arizona, 2004.

[34] A Vernet, GA Kopp, JA Ferré, and F Giralt. Three-dimensional structure and momentum transfer in a turbulent cylinder wake. *J. Fluid Mech.*, 394:303–373, 1999.

[35] A Töpler. *Beobachtungen nach der Schlierenmethode*. Leipzig: Engelmann, 1906.

[36] CJ Bourdon and JC Dutton. Planar visualizations of large-scale turbulent structures in axisymmetric supersonic separated flows. *Phys. Fluids*, 11:201–213, 1998.

[37] LM Mack. Boundary-layer linear stability theory. AGARD Report 709, Advisory Group for Aerospace Research and Development, 1984.

[38] CW Rowley, T Colonius, and RM Murray. Model reduction for compressible flows using POD and Galerkin projection. *Physica D*, 189:115–129, 2004.

[39] FM White. *Viscous Fluid Flow*. McGraw Hill, 1991.

[40] RD Sandberg. *Numerical Investigation of Transitional and Turbulent Supersonic Axisymmetric Wakes*. PhD thesis, The University of Arizona, 2004.

[41] CHK Williamson. Vortex dynamics in the cylinder wake. *Ann. Rev. Fluid Mech.*, 28:477–539, 1996.

[42] D Barkley and RD Henderson. Three-dimensional Floquet stability analysis of the wake of a circular cylinder. *J. Fluid Mech.*, 322:215–241, 1996.

[43] RD Henderson. Nonlinear dynamics and pattern formation in turbulent wake transition. *J. Fluid Mech.*, 352:65–112, 1997.

[44] RD Sandberg and HF Fasel. Numerical investigation of transitional supersonic axisymmetric wakes. *J. Fluid Mech.*, 563:1–41, 2006.

[45] PS Klebanoff, KD Tidstrom, and LM Sargent. The three-dimensional nature of boundary-layer instability. *J. Fluid Mech.*, 12:1–34, 1962.

Figures

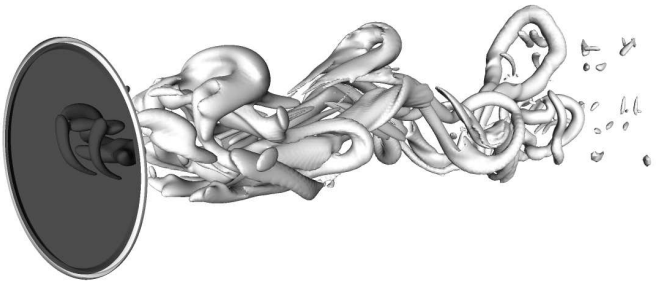

Figure 1: Perspective view of instantaneous contours of $Q = 0.2$; the dark shaded area indicates the base of the body; $Re_D = 2 \times 10^3$, $Ma = 0.25$.

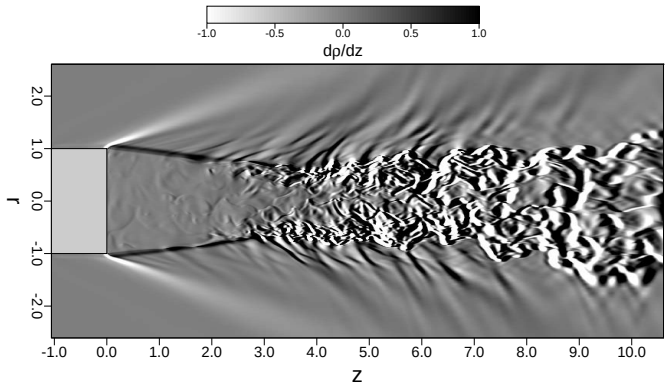

Figure 2: Sideview of instantaneous streamwise density-gradient; $Re_D = 10^5$, $Ma = 2.46$.

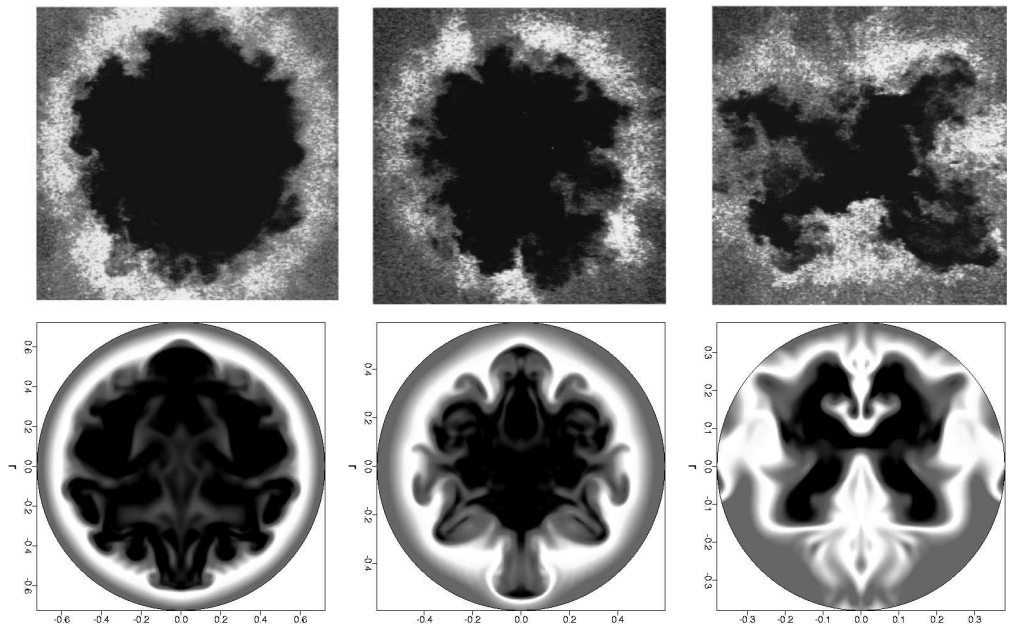

Figure 3: Visualisation using Mie-scattering from experiments [36] at $Re_D = 3.3 \times 10^6$ (top) and using contours of instantaneous local Mach number from DNS data at $Re_D = 10^5$ (bottom); $Ma = 2.46$; endviews at locations C, D and E in the experiments and comparable streamwise locations in the DNS are shown from left to right.

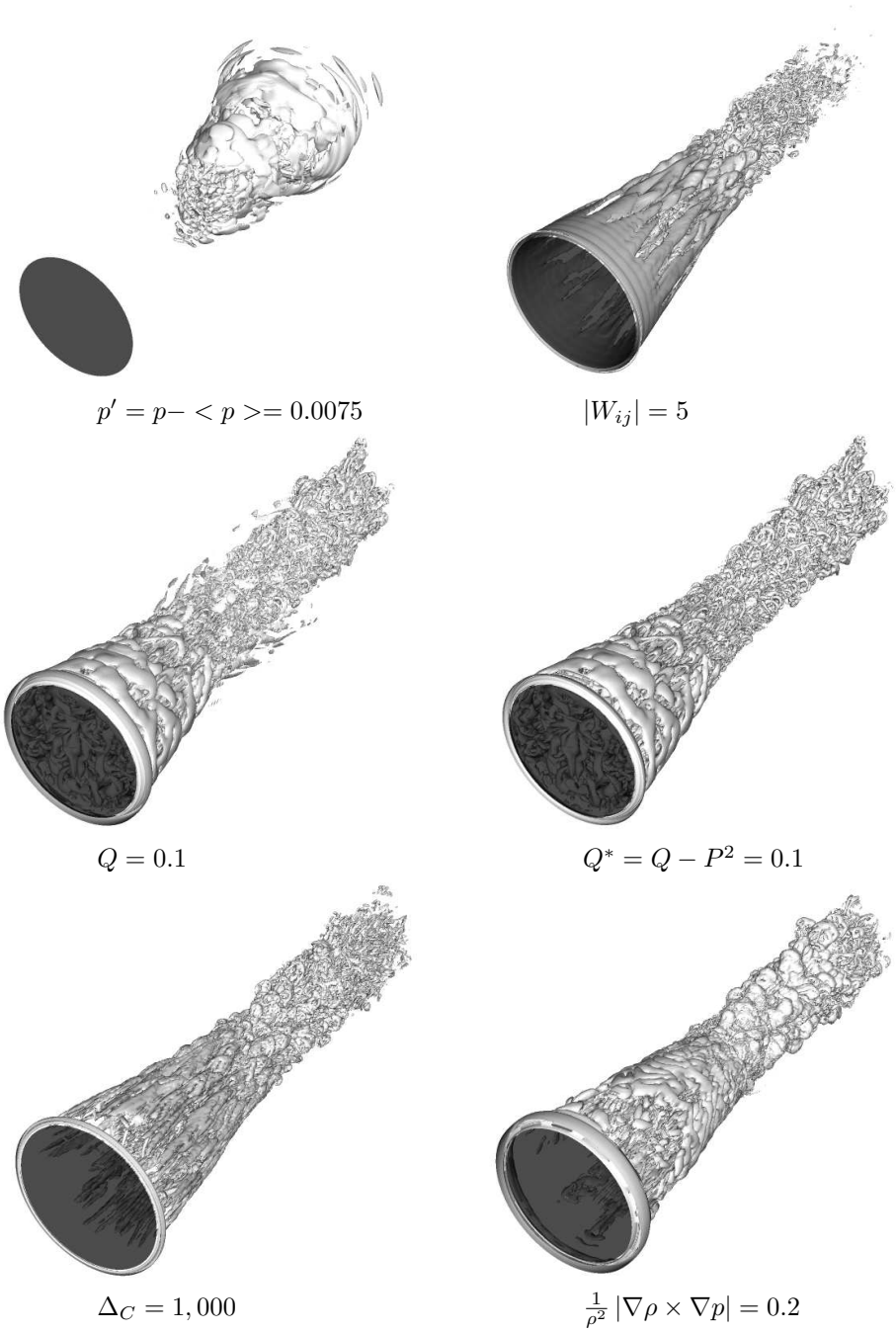

Figure 4: Perspective views of different visualisation methods applied to instantaneous data of the compressible axisymmetric wake; the dark shaded area indicates the base of the body; $Re_D = 10^5$, $Ma = 2.46$.

Figure 5: Perspective views of instantaneous contours of $Q = 0.1$ of the unforced (left) and forced (right) flow; the dark shaded area indicates the base of the body; $Re_D = 3 \times 10^4$, $Ma = 2.46$.

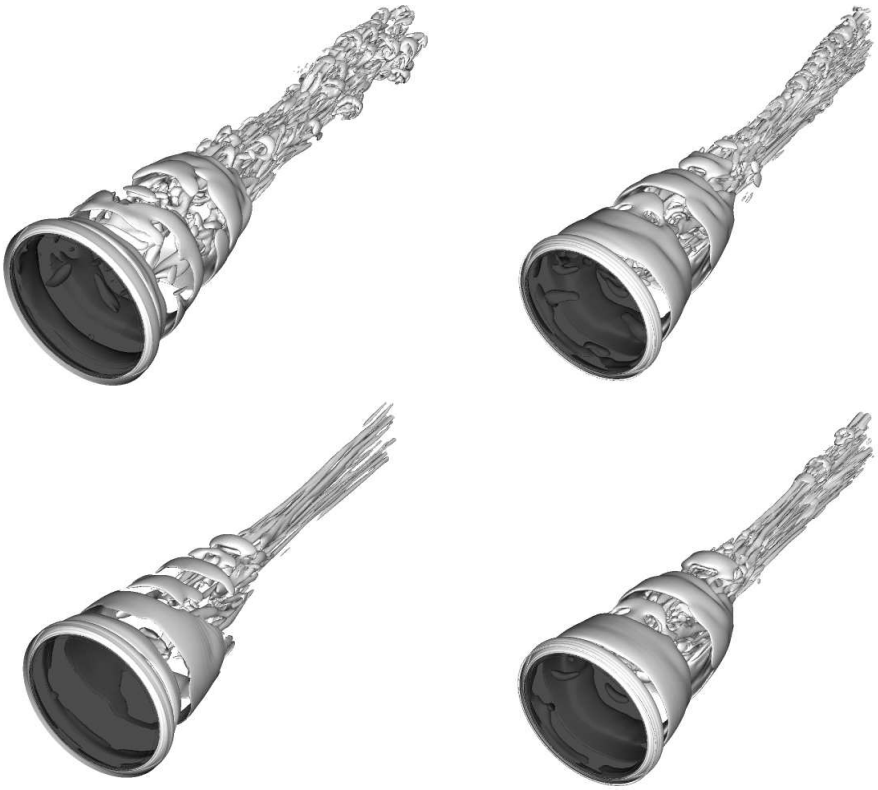

Figure 6: Perspective views of instantaneous contours of Q of the instantaneous flow (top left) and approximations of this flow field using POD-modes 1 to 32 (top right), POD-mode 1 (bottom left) and POD-modes 1 to 5 (bottom right); the dark shaded area indicates the base of the body; periodic forcing with $St = 0.83$, $Re_D = 3 \times 10^4$, $Ma = 2.46$.

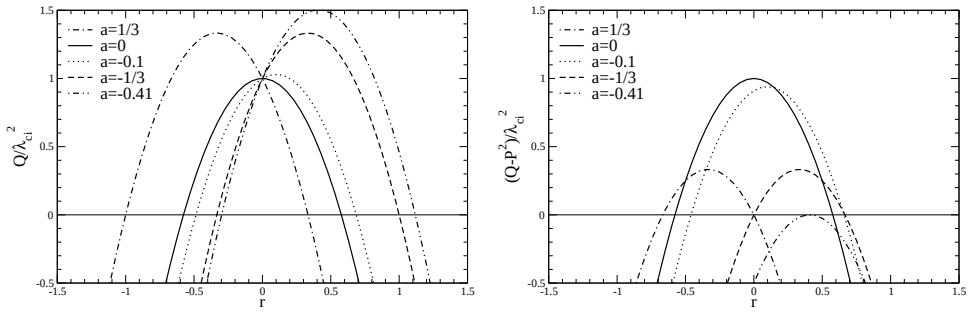

Figure 7: Range of valid inverse spiralling compactness r for compressible (left) and incompressible (right) form of the Q-criterion for different values of the vortex compressibility parameter a.

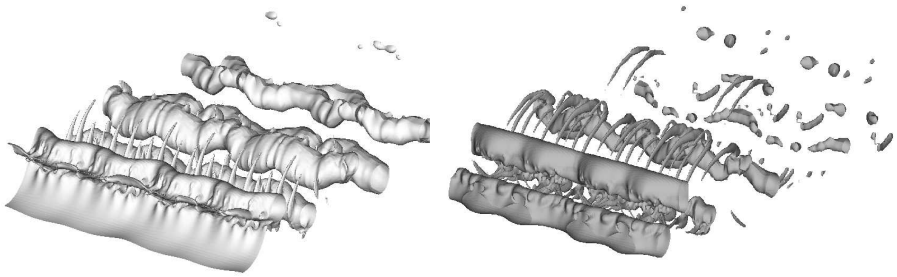

Figure 8: Perspective views of instantaneous total and disturbance pressure contours of the near wake behind a two-dimensional bluff body: $p = 0.99\ p_\infty$ (left), $p' = p - < p >= -0.005\ p_\infty$ (right); flow from lower left to upper right, $0 \leq x \leq 20$, $-3.9 \leq y \leq 3.9$, $-4 \leq z \leq 4$, $Re_D = 10^3$, $Ma = 0.25$.

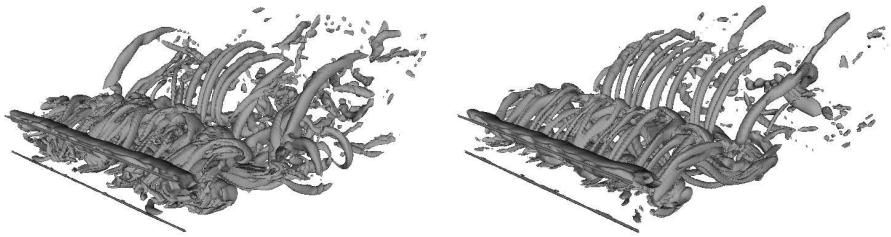

Figure 9: Perspective views of instantaneous contours of $Q = 2$ for two instants in time of the near wake behind a two-dimensional bluff body, flow from lower left to upper right, $0 \leq x \leq 10$, $-3.9 \leq y \leq 3.9$, $-4 \leq z \leq 4$, $Re_D = 10^3$, $Ma = 0.25$.